Electronic Supplementary Information *for*

An insight into thermo-thickening behavior of wormlike micellar solutions based on ultra-long-chain surfactants

Quan Yin,[a] Qiang Tian,[b] James Doutch,[c] Asante O. Frimpong,[d] Xiao Xu,[d] Hongyao Yin,[a] Peixun Li,[c,*] Yujun Feng[a,*]

[a] *Polymer Research Institute, State Key Laboratory Polymer Materials Engineering, Sichuan University, Chengdu 610065, China*

[b] *State Key Laboratory of Environment-Friendly Energy Materials, School of Materials Science and Engineering, Southwest University of Science and Technology, Mianyang 621010, China*

[c] *ISIS Neutron and Muon Source, Science and Technology Facilities Council, Rutherford Appleton Laboratory, Didcot, OXON OX11 0QX, UK*

[d] *School of Chemistry and Chemical Engineering, Nanjing University of Science and Technology, Nanjing 210094, China*

**Corresponding author at: peixun.li@stfc.ac.uk (P. Li), yjfeng@scu.edu.cn (Y. Feng)*

Characterization of five ultra-long-chain surfactants

The purity of five ultra-long-chain surfactants was confirmed by high performance liquid chromatography (HPLC) (**Figures S1–S5**).

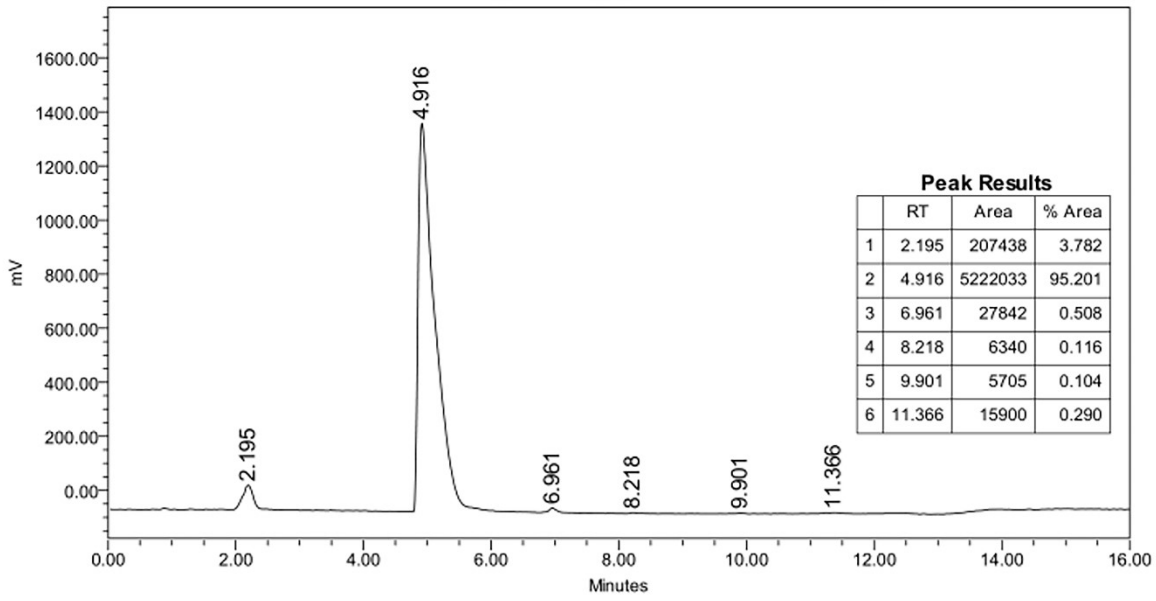

Fig. S1. HPLC result of $UC_{22}DAI$.

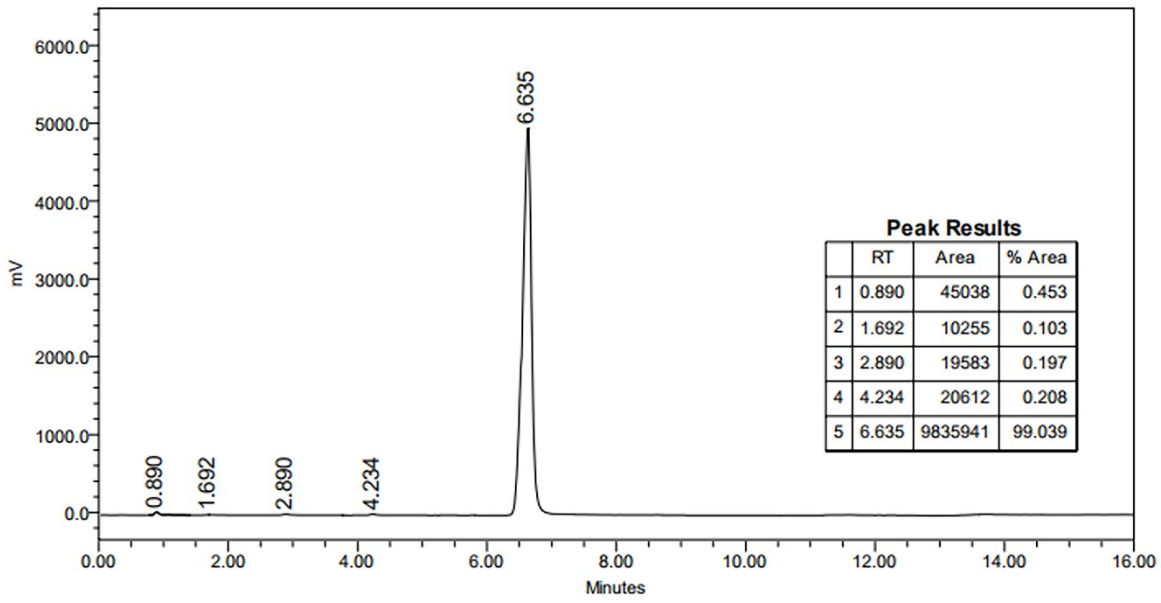

Fig. S2. HPLC result of $UC_{22}DAB$.

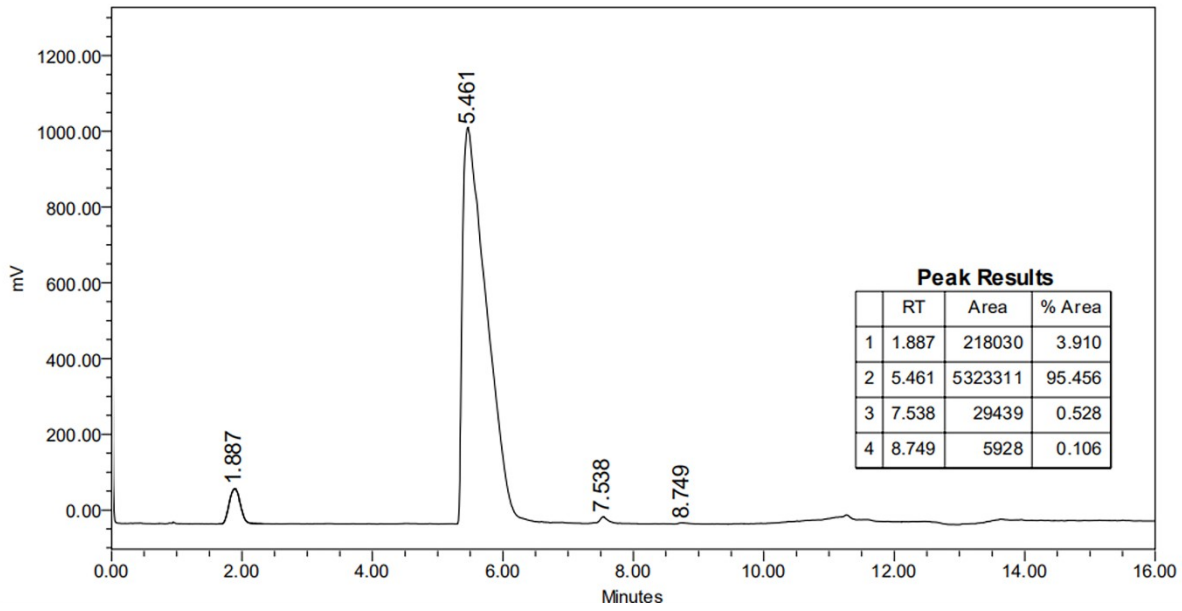

Fig. S3. HPLC result of $UC_{22}DAS$.

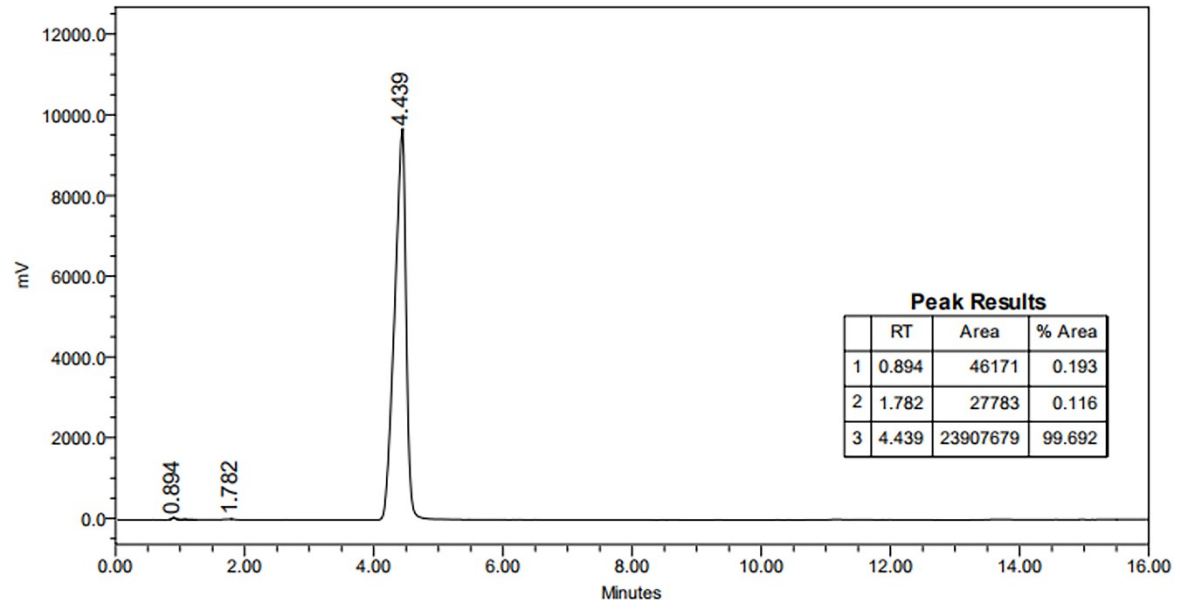

Fig. S4. HPLC result of $UC_{18}DAS$.

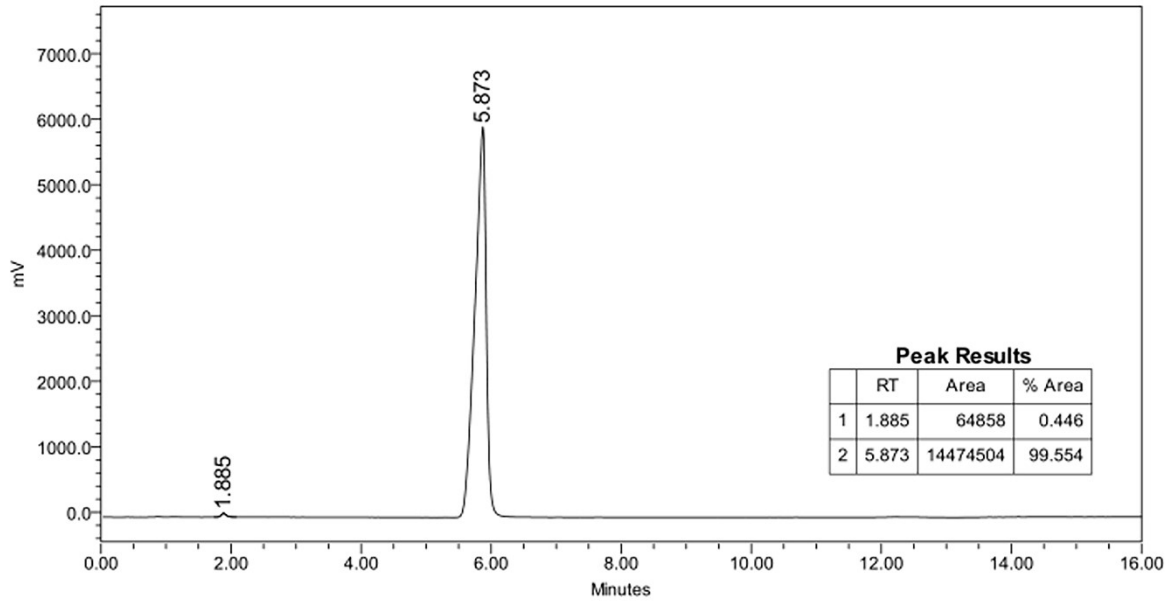

Fig. S5. HPLC result of C_{18}DAS.

Photographs of the solutions at characteristic temperature

The five surfactant solutions were heated at different temperatures at least for 0.5 h. Then, we observed and photographed the appearance of five surfactant solutions at different temperatures. All the solution were optically clear and isotropic over the test temperature range (**Fig. S6**)

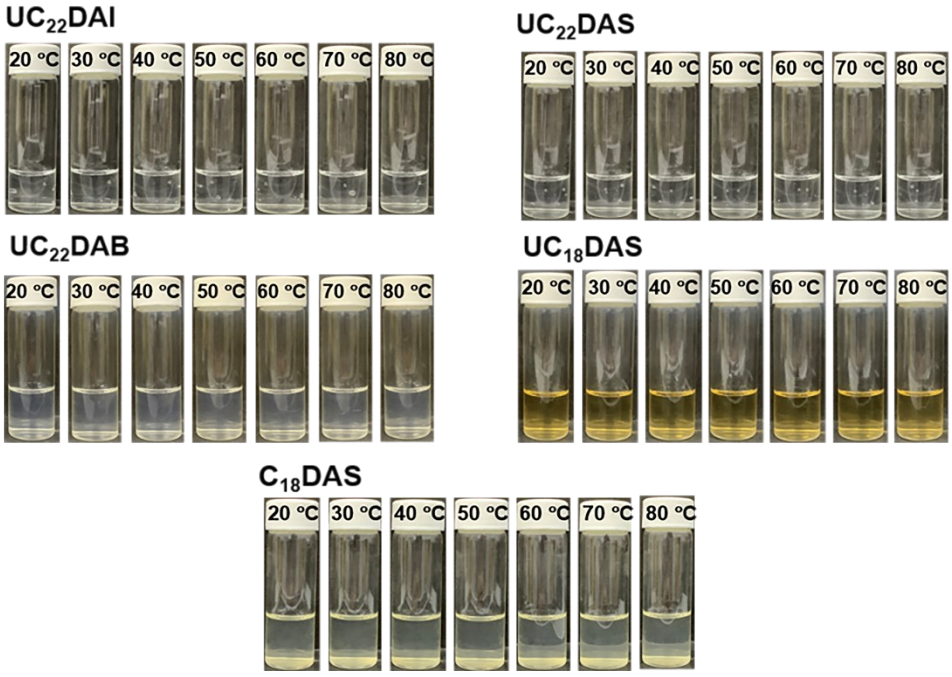

Fig. S6. Snapshots of the solutions of five ultra-long-chain surfactants at different temperatures.

The results and discussion of molecular dynamic simulation

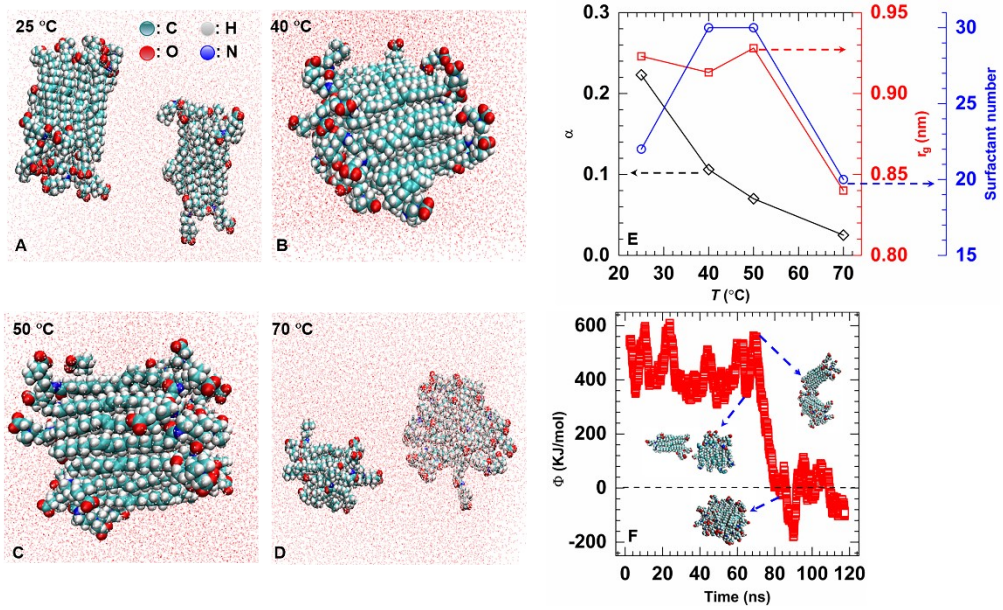

Fig. S7. Simulation snapshots of the equilibrated micellar structures of $UC_{22}DAB$ molecules at (A) 25 °C, (B) 40 °C, (C) 50 °C and (D) 70 °C. (E) The variation of asphericity (α), radius of gyration and the number of $UC_{22}DAB$ molecules inside micelle with temperature; (F) the calculated potential energy (ϕ) of $UC_{22}DAB$ micelles at 50 °C.

To gain further understanding of the thermo-thickening behavior of $UC_{22}DAB$ solution, MD simulations were performed at representative temperatures in Fig. 1A, 25, 40, 50, and 70 °C, respectively, and the simulation snapshots of the equilibrated micellar structures are depicted in **Fig. S7**. The micelle in this work is artificially defined as a cluster with more than five $UC_{22}DAB$ molecules. As shown in Fig. 7A, the $UC_{22}DAB$ molecules self-assembles into two short rod-like micelles at 25 °C. At 40 and 50 °C, we find all the 30 $UC_{22}DAB$ molecules fuse into a large micelle (Figs. 7B and C). It just took 5 ns to create the large micelle at 50 °C, much earlier than that at 40 °C (17 ns), indicating that high temperature accelerates micellar aggregation. However, at 70 °C (Fig. 7D), the simulated 30 surfactants end up forming two micelles; furthermore, the combination of these two micelles does not happen even when we extend the simulation to 200 ns, which suggests that aggregation is a relatively unfavorable process at higher temperature.

We calculated the average radius of gyration (r_g) of the $UC_{22}DAB$ micelles in the simulation at four different temperatures. It was determined that the micelles are well extended from 25 °C to 50 °C with r_g of around 0.91 nm, while a marked decrease of r_g (0.84 nm) is found at 70 °C, signifying the coil-like structure. The structural change of the surfactant corresponds well with the evolution of the micelles. Thus, “unbreakable” wormlike micelles were found below 50 °C, as opposed to the short rod-like micelles and even spherical micelles formed by wormlike micelles fracture which were observed at 70 °C. This smooth structure change from rod to spherical is better illustrated by a calculation of the micelle asphericity (α), which is used to describe micellar morphology. The degree of asphericity (α) of micelles is defined in terms of the eigenvalue λ_i^2, which can be written as:

$$\alpha = \frac{\langle (T_r^2 - 3M) \rangle}{T_r^2}$$

(1)

with $T_r = \lambda_1^2 + \lambda_2^2 + \lambda_3^2$, $M = \lambda_1^2\lambda_2^2 + \lambda_2^2\lambda_3^2 + \lambda_1^2\lambda_3^2$ and $\langle \ldots \rangle$ stands for the ensemble average. For a perfect sphere α equals 0, whereas $\alpha = 1$ corresponds to the extreme of an infinitely thin rod. This result in Fig. S7E corresponds well to the estimate of the surfactant number counted in the biggest micelle, for which the larger aggregation number of surfactants observed from 25 °C to 50 °C results in a rod-like micelle with smaller asphericity. Note that, it is generally unfeasible to combine two spherical micelles, given the like-charged and hydrophilic oxygen atoms that cover the micelle surface. As a result, the micelles do not favour stepwise growth at 70 °C.

The current results still cannot rationalize our simulations at 25 °C, given the fact that the maximum micelle size (Fig. S7E) at this temperature is smaller, whereas the observed r_g and the asphericity factor at this temperature is indeed similar with those at 40 and 50 °C. We therefore examined the behaviour of the system potential energy (ϕ) measured at 50 °C (Fig. S7F). A sharp decrease of ϕ with a magnitude of 400 kJ·mol^{-1} occurs in the simulation which is mostly contributed from the energy gain in joining the hydrophobic interface of two micelles. Prior to this jump, we also find an energy barrier of 150 kJ·mol^{-1} before the equilibrated structure of the bigger micelle is reached. Possible reasons for this energy barrier are the electrostatic repulsions of the densely packed charged groups of the surfactant, and possibly more importantly, from a subtle effect of the self-adjustment of the micelle to extend its hydrophobic surface before joining with another micelle. Overcoming this energy barrier will be easier at high temperatures, whereas at lower temperatures (such as 25 °C) the micelles have less flexibility and a high bending modulus. The simulation results indicate the presence of a range of temperatures between 40 °C and 50 °C where the underlying $UC_{22}DAB$ have a better chance of forming larger micelles, and possibly of a denser wormlike micellar network.

Additional Rheological results

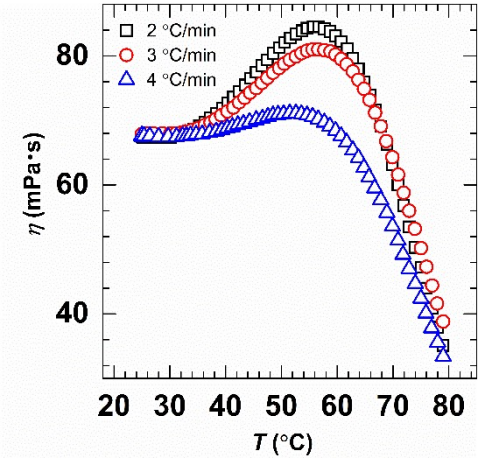

Fig. S8. Temperature dependence of apparent viscosity of $UC_{22}DAB$ aqueous solutions at different heating rate.

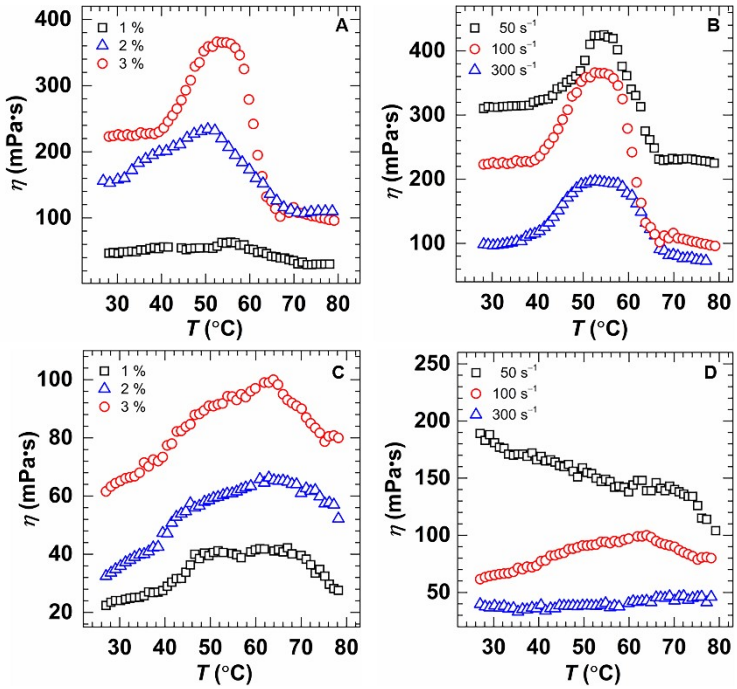

Fig. S9. Effect of concentration on thermo-thickening behavior of (A) $UC_{22}DAB$ and (C) $UC_{22}DAI$ at fixed shearing rate of 100 s^{-1}; effect of shearing rate on thermo-thickening behavior of (B) $UC_{22}DAB$ and (D) $UC_{22}DAI$ at fixed concentration of 3 %.

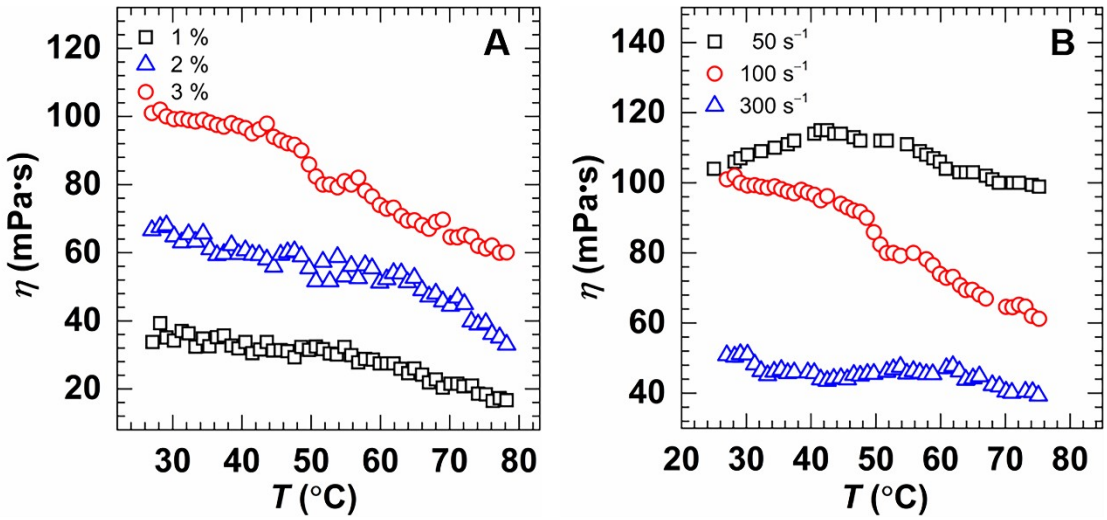

Fig. S10. Temperature dependence on apparent viscosity of (A) series concentration $UC_{22}DAS$ at 100 s^{-1} and (B) 3 % $UC_{22}DAS$ at various shear rates.

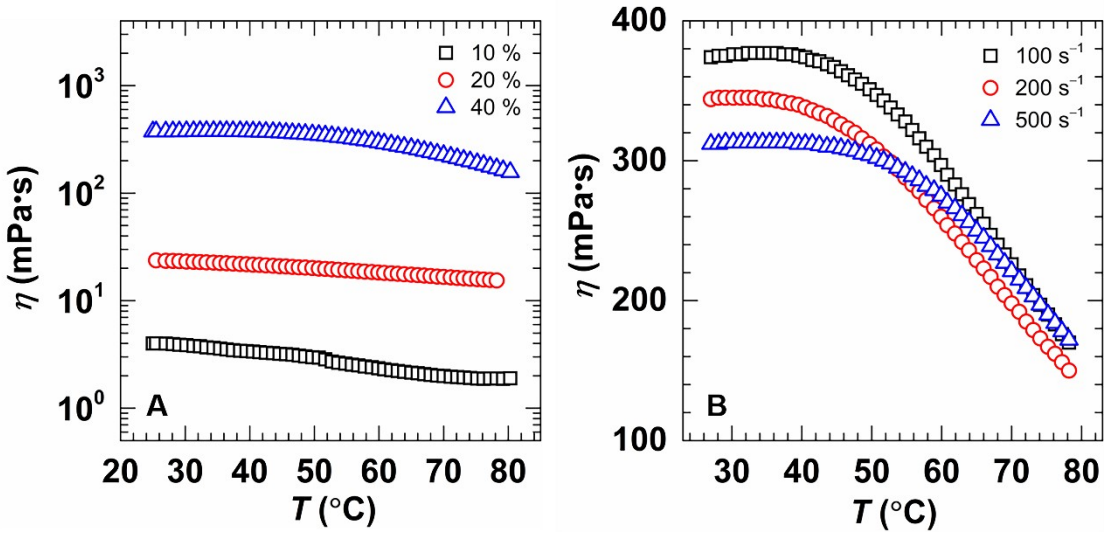

Fig. S11. Temperature dependence on apparent viscosity of (A) series concentration $UC_{18}DAS$ at 100 s^{-1} and (B) 40 % $UC_{18}DAS$ at various shear rate.

The Rheo-SANS, SAXS and Molecular dynamics simulation results

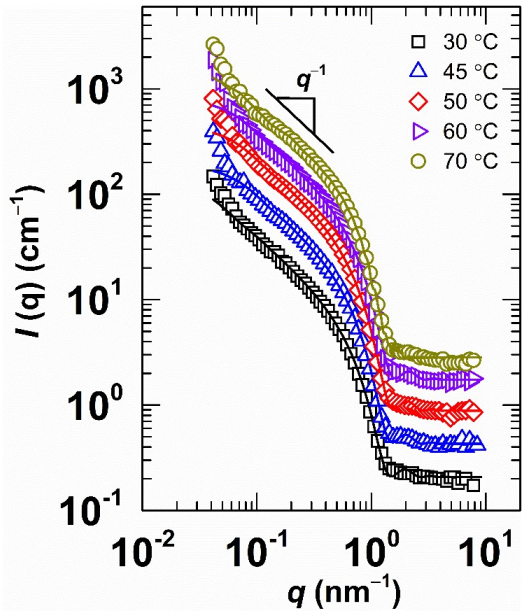

Fig. S12. Rheo-SANS data of 3.0% $UC_{22}DAB$ at 100 s^{-1}. For better visibility the $I(q)$ vs q curves are scaled vertically by factors of 2 (45 °C), 4 (50 °C), 8 (60 °C) and 12 (70 °C). The solid lines are the best fits to cylinder model.

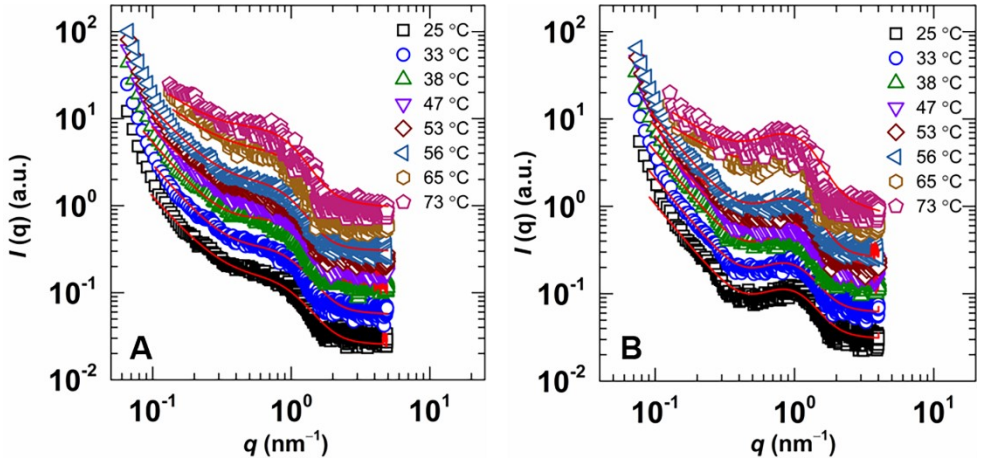

Fig. S13. SAXS data of 3% (A)$UC_{22}DAB$ and (B)$UC_{22}DAI$ at various temperatures. For better visibility, the $I(q)$ vs q curves of high temperatures (> 25 °C) in A and B are scaled vertically by factors of 2, 4, 6, 8, 10, 20 and 30. The red solid lines are the best fits to worm model.

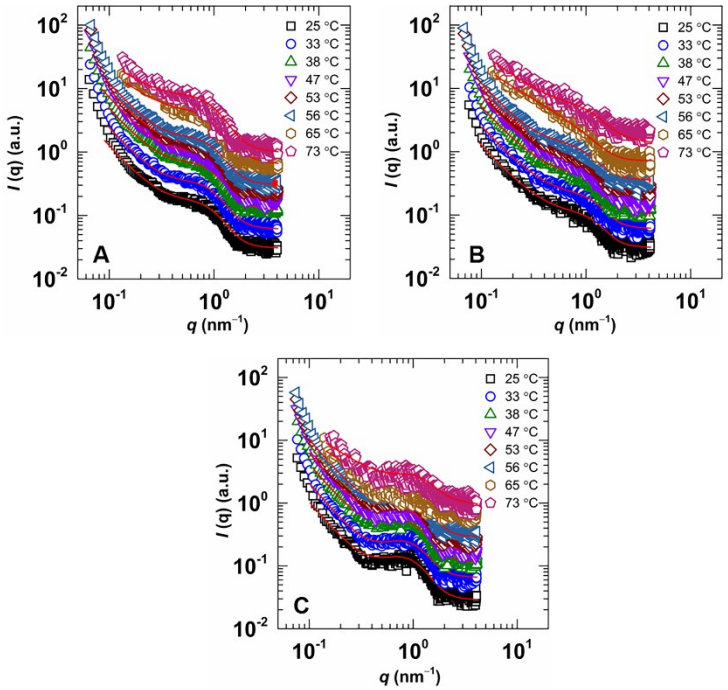

Fig. S14. SAXS data of 3% (A)$UC_{22}DAB$, (B)$UC_{22}DAI$ and (C) $UC_{22}DAS$ solutions at various temperatures. For better visibility, the $I(q)$ vs q curves of high temperatures (> 25 °C) in A, B and C are scaled vertically by factors of 2, 4, 6, 8, 10, 20 and 30. The red solid lines are the best fits to worm model.

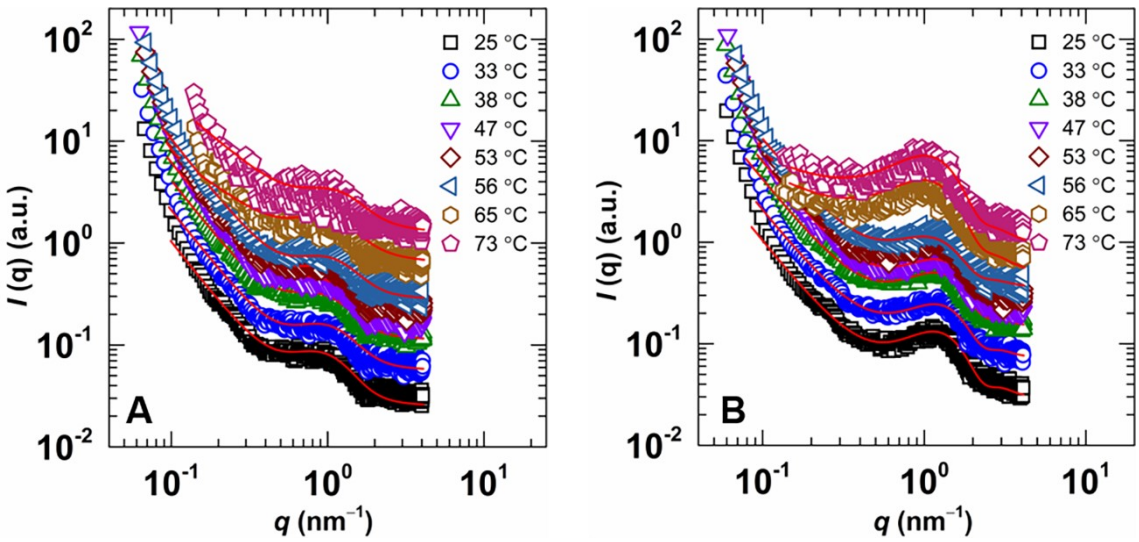

Fig. S15. SAXS data of (A) 1% $UC_{22}DAS$ and (B) 20% $UC_{18}DAS$ solutions at various temperatures. For better visibility, the $I(q)$ vs q curves of high temperatures (> 25 °C) in A and B are scaled vertically by factors of 2, 4, 6, 8, 10, 20 and 30. The red solid lines are the best fits to worm model.

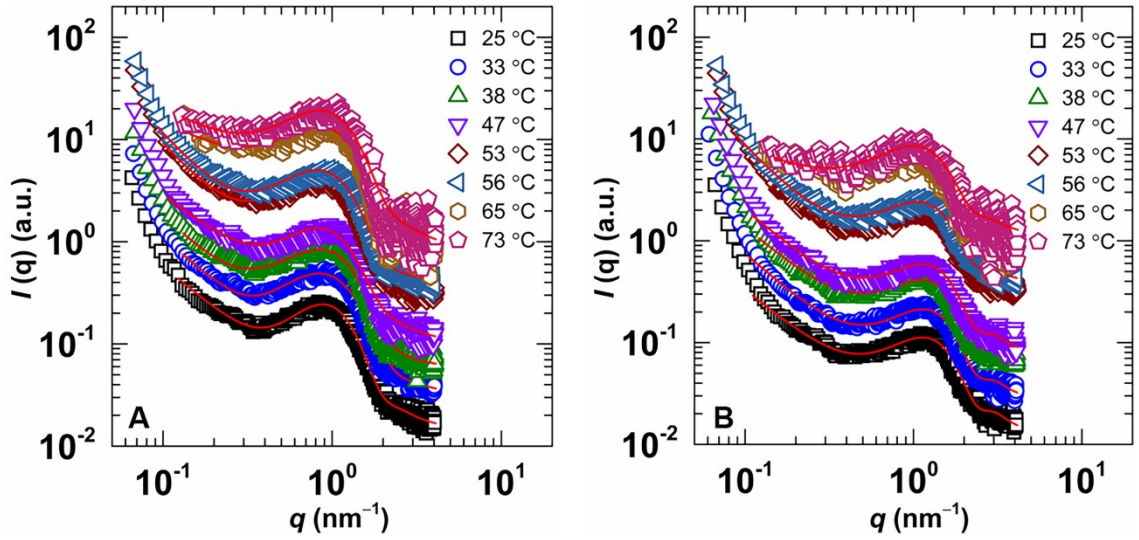

Fig. S16. SAXS data of 10% (A) $C_{18}DAS$ and (B) $UC_{18}DAS$ solutions at various temperatures. For better visibility, the $I(q)$ vs q curves of high temperatures (> 25 °C) in A and B are scaled vertically by factors of 2, 4, 6, 8, 10, 20 and 30. The red solid lines are the best fits to worm model.

Table S1. Structural parameters obtained from Rheo-SANS data on $UC_{22}DAB$ solution by curve fitting using cylinder model

T (°C)	Radius (nm)	Distribution of Radius	Persistence Length (nm)	Fit Error (nm)	Volume Fraction	Reduced χ^2
30	2.5	0.146	84.9	2.1	0.073	2.4
45	2.5	0.096	52.1	1.7	0.095	6.9
50	2.4	0.080	55.7	2.0	0.111	13.2
60	2.4	0.058	61.4	2.1	0.105	14.0
70	2.4	0.085	47.4	1.5	0.125	12.7

Table S2. Characteristic parameters for 10% $C_{18}DAS$ solution at different shear rate

Shear rate (s^{-1})	η_{ini} (mPa·s)	η_{max} (mPa·s)	T_s (°C)	T_c (°C)	k
5	1.6	1210	42.5	71.1	63.6
10	1.5	443	42.5	70.9	22.7
100	1.6	231	42.6	71.1	13.1
300	1.6	195	42.6	72.1	10.9
500	1.7	141	42.5	72.1	7.5

η_{ini}: the initial viscosity;

η_{max}: the maximum viscosity;

T_s: the temperature at which viscosity starts to increase;

T_c: the temperature at which viscosity reaches maximum;

k: the temperature sensitive factor.

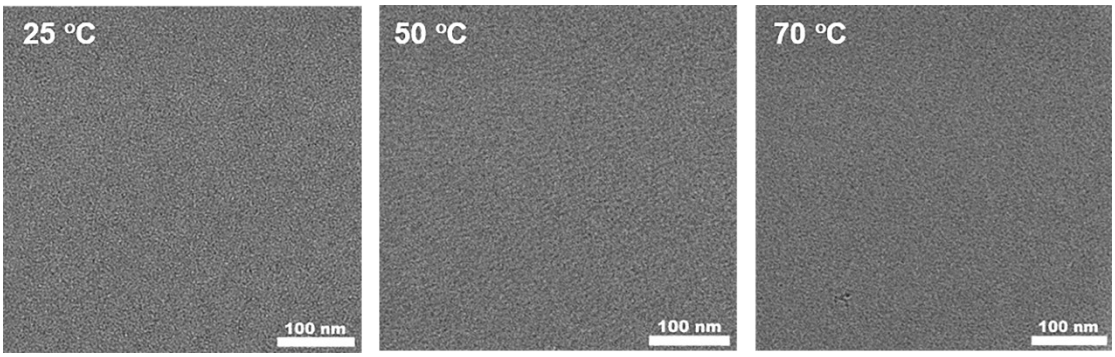

Fig. S17. Cryo-TEM images of the 10 % $UC_{18}DAS$ solution at various temperatures.

The SAXS data was fitted to “worm-chain” model by SASfit software. The scattering vector q is defined as:

$$q = (4\pi/\lambda)\sin\theta \tag{1}$$

in which λ is the wavelength of the X-rays, and 2θ is the scattering angle. The scattering intensity $I(q)$ is generally described by:

$$I(q) = nP(q)S(q) \tag{2}$$

where n is the total number of particles, and P(q) and S (q) are the form and structure factors.

The form factors for wormlike micelles are approximated by the form factor of the Kholodenko-worm where the scattering length density profile across the wormlike segments are described by those of a rodlike micelle. The corresponding function are given by:

$$P_{\text{core}}(q,R_{\text{core}},l,L) = P_{\text{worm}}(q,l,L)P_{\text{cs}}(q,R_{\text{core}},d,R_{\text{g}}) \tag{3}$$

The contribution of the wormlike conformation of the micelle P_{worm} (q,l,L) is described by the formula of Kholodenko for wormlike structures. The contribution of the cross-section P_{cs} is the same as for rodlike micelles and given by

$$P_{\text{cs}}(q,R_{\text{core}},d,R_{\text{g}}) = \left[\frac{2J_1(qR_{\text{core}})}{qR_{\text{core}}}\right]^2 \tag{4}$$

$$Si(x) = \int_0^x t^{-1}\sin t\,dt \tag{5}$$

$$P_{\text{brush}}(q,R_{\text{g}}) = 2\frac{exp(-x) - 1 + x}{x^2} \text{ with } x = R_{\text{g}}^2q^2 \tag{6}$$

$$S_{\text{brush - core}}(q,R_{\text{core}},l,L,R_{\text{g}},d) = \psi(q,R_{\text{g}}) \times \frac{2J_1(qR_{\text{core}})}{qR_{\text{core}}} J_0\left[q\left(r_{\text{core}} + dR_{\text{g}}\right)\right]P_{\text{worm}}(q,l,L) \tag{7}$$

$$S_{\text{brush - brush}}(q,R_{\text{core}},l,L,d,R_{\text{g}}) = \psi^2(qR_{\text{g}})J_0^2\left[q\left(r_{\text{core}} + dR_{\text{g}}\right)\right]P_{\text{worm}}(q,l,L) \tag{8}$$

The excess scattering lengths and aggregation number are given by:

$$\beta_{\text{core}} = V_{\text{core}}(\eta_{\text{core}} - \eta_{\text{solv}}) \tag{9}$$

$$\beta_{\text{brush}} = V_{\text{brush}}(\eta_{\text{brush}} - \eta_{\text{solv}}) \tag{10}$$

$$N_{\text{agg}} = (1 - x_{\text{solv,core}})\pi R_{\text{core}}^2 L/V_{\text{core}} \tag{11}$$

The parameters are:

R_{core}: core radius

V_{core}: molecular volume of single block unit in the micellar core

V_{brush}: molecular volume of single block unit in the micellar corona

η_{core}: scattering length density of spherical core

η_{brush}: scattering length density of the block unit in the corona

η_{solv}: scattering length density of solvent

$\text{xsolv}_{\text{core}}$: amount of solvent in core

R_g: gyration radius of polymer chains in the corona
l: Kuhn length of the wormlike of the micelle
L: contour length of the wormlike of the micelle

The description of logistic function in Fig. 5A:

$$y = A_2 + \frac{A_1 - A_2}{1 + (\frac{x}{x_0})^p} \tag{12}$$

It can be converted into:

$$\frac{y - A_2}{A_1 - A_2} = \frac{1}{1 + (\frac{x}{x_0})^p} \tag{13}$$

where, the A_1 is the minimum value of logistic function, A_2 is the maximum value, x_0 is the center and the p is the power index. The result of fitting with logistic function is shown in Fig. S18, here, the η, T, η_{min}, η_{max}, T_0 are y, x, A_1, A_2, x_0 respectively. Thus, function (19) can be written as:

$$\frac{\eta - \eta_{max}}{\eta_{min} - \eta_{max}} = \frac{1}{1 + (\frac{T}{T_0})^p} \tag{14}$$

where, the η_{min} is the minimum viscosity, η_{max} is the maximum viscosity, respectively, T_0 is the center temperature and the p is the power index. And the viscosity at T_0 satisfies the following formula:

$$\eta(T_0) = \frac{\eta_{max} + \eta_{min}}{2} \tag{15}$$

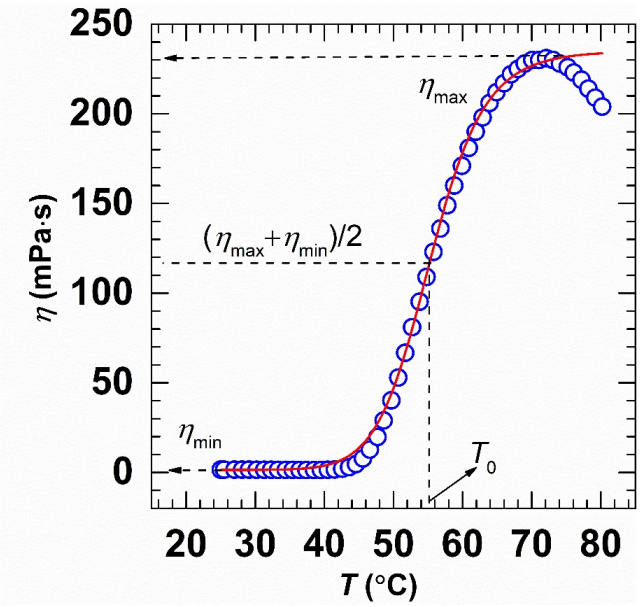

Fig. S18 Temperature dependence of apparent viscosity of 10% C_{18}DAS. The solid line is fitted by logistic function.

Table S3. Fitting parameters for the size distribution and formfactor of "worm-chain" model

Sample	T (°C)	R_{core} (nm)	V_{core}	V_{brush}	R_g (nm)	l (nm)	L (nm)
3% UC22DAB (without NaCl)	25	2.5	0.6	0.1331	1.4	52	> 100
	33	2.5	0.6	0.121	1.6	52	> 100
	38	2.5	0.6	0.1331	1.4	55	> 100
	47	2.5	0.6	0.11	1.6	58	> 100
	53	2.5	0.6	0.1331	1.4	60	> 100
	56	2.5	0.6	0.1331	1.4	60	> 100
	65	2.5	0.6	0.1331	1.4	55	> 100
	73	2.5	0.6	0.1331	1.4	51	> 100
3% UC22DAI (without NaCl)	25	2.9	0.6	0.132	1.3	55	> 100
	33	2.9	0.6	0.132	1.3	57	> 100
	38	2.9	0.6	0.132	1.3	59	> 100
	47	2.9	0.6	0.132	1.3	59	> 100
	53	2.9	0.6	0.132	1.2	60	> 100
	56	2.9	0.6	0.132	1.3	61	> 100
	65	2.9	0.6	0.132	1.3	56	> 100
	73	2.9	0.6	0.132	1.3	49	> 100
3% UC22DAB	25	2.5	0.6	0.1461	1.44	46	> 100
	33	2.5	0.6	0.1461	1.44	46	> 100
	38	2.5	0.6	0.1461	1.44	51	> 100
	47	2.5	0.6	0.1461	1.44	53	> 100
	53	2.5	0.6	0.1461	1.44	56	> 100
	56	2.5	0.6	0.1461	1.44	57	> 100
	65	2.5	0.6	0.1461	1.44	50	> 100
	73	2.5	0.6	0.1461	1.44	48	> 100
3% UC22DAI	25	2.9	0.6	0.16	0.73	63	> 100
	33	2.9	0.6	0.16	0.73	60	> 100
	38	2.9	0.6	0.16	0.73	59	> 100
	47	2.9	0.6	0.16	0.73	55	> 100
	53	2.9	0.6	0.16	0.73	54	> 100
	56	2.9	0.6	0.16	0.73	54	> 100
	65	2.9	0.6	0.16	0.73	52	> 100
	73	2.9	0.6	0.16	0.73	50	> 100
3% UC22DAS	25	2.8	0.6	0.1947	1.3	50	> 100
	33	2.8	0.6	0.1947	1.3	51	> 100
	38	2.8	0.6	0.1947	1.3	52	> 100
	47	2.8	0.6	0.1947	1.3	51	> 100
	53	2.8	0.6	0.1947	1.3	50	> 100
	56	2.8	0.6	0.1947	1.3	51	> 100
	65	2.8	0.6	0.1947	1.3	48	> 100
	73	2.8	0.6	0.1947	1.3	45	> 100
1% UC22DAS	25	2.8	0.6	0.2848	1.19	37	> 100
	33	2.8	0.6	0.2848	1.19	40	> 100
	38	2.8	0.6	0.2848	1.19	42	> 100
	47	2.8	0.6	0.2848	1.19	43	> 100
	53	2.8	0.6	0.2848	1.19	43	> 100
	56	2.8	0.6	0.2848	1.19	44	> 100
	65	2.8	0.6	0.2848	1.19	42	> 100
	73	2.8	0.6	0.2848	1.19	38	> 100
20% UC18DAS	25	2.3	0.6	0.1089	0.1	1.8	4.5
	33	2.3	0.6	0.1089	0.1	1.7	4
	38	2.3	0.6	0.1089	0.1	1.7	4.1
	47	2.3	0.6	0.1089	0.1	1.7	3.8

Sample	T (°C)	R_{core} (nm)	V_{core}	V_{brush}	R_g (nm)	l (nm)	L (nm)
	53	2.3	0.6	0.1089	0.1	1.7	3.6
	56	2.3	0.6	0.1089	0.1	1.7	3.6
	65	2.3	0.6	0.1089	0.1	1.7	3.6
	73	2.3	0.6	0.1089	0.1	1.7	3.6
10%	25	2.3	0.6	0.1089	0.1	1.8	4.4
UC18DAS	33	2.3	0.6	0.1089	0.1	1.8	4.2
	38	2.3	0.6	0.1089	0.1	1.7	4
	47	2.3	0.6	0.1089	0.1	1.7	3.9
	53	2.3	0.6	0.1089	0.1	1.6	3.9
	56	2.3	0.6	0.1089	0.1	1.6	3.9
	65	2.3	0.6	0.1089	0.1	1.6	3.9
	73	2.3	0.6	0.1089	0.1	1.6	3.9
10%	25	2.2	0.6	0.1089	0.1	2.7	6.6
C18DAS	33	2.2	0.6	0.1089	0.1	5.8	19
	38	2.2	0.6	0.1089	0.1	8.3	33
	47	2.2	0.6	0.1089	0.1	30	43
	53	2.2	0.6	0.1089	0.1	45	> 100
	56	2.2	0.6	0.1089	0.1	50	> 100
	65	2.2	0.6	0.1089	0.1	55	> 100
	73	2.2	0.6	0.1089	0.1	50	> 100